



## Full length article

# Mechanical properties of stingray tesseræ: High-resolution correlative analysis of mineral density and indentation moduli in tessellated cartilage



Ronald Seidel<sup>a,i,1</sup>, Andreas Roschger<sup>a,b,1</sup>, Ling Li<sup>c,d,e,1,2</sup>, Joseph J. Bizzarro<sup>f</sup>, Qiuting Zhang<sup>g</sup>, Jie Yin<sup>g</sup>, Ting Yang<sup>e</sup>, James C. Weaver<sup>d</sup>, Peter Fratzl<sup>a</sup>, Paul Roschger<sup>h</sup>, Mason N. Dean<sup>a,\*</sup>

<sup>a</sup> Max Planck Institute of Colloids and Interfaces, Department of Biomaterials, Am Muehlenberg 1, 14424 Potsdam, Germany

<sup>b</sup> Paris-Lodron-University of Salzburg, Department of Chemistry and Physics of Materials, 5020 Salzburg, Austria

<sup>c</sup> John A. Paulson School of Engineering and Applied Sciences, Harvard University, Cambridge, MA 02138, USA

<sup>d</sup> Wyss Institute for Biologically Inspired Engineering, Harvard University, Cambridge, MA 02138, USA

<sup>e</sup> Department of Mechanical Engineering, Virginia Tech, 635 Prices Fork Road, Blacksburg, VA 24060, USA

<sup>f</sup> Institute of Marine Sciences, University of California, Santa Cruz, CA 95060, USA

<sup>g</sup> Department of Mechanical Engineering, Temple University, Philadelphia, PA 19122, USA

<sup>h</sup> Ludwig Boltzmann Institute of Osteology at the Hanusch Hospital of WGKK and AUVA, Trauma Centre Meidling, 1st Medical Dept., Hanusch Hospital, Vienna, Austria

<sup>i</sup> B CUBE, Center for Molecular Bioengineering, Tatzberg 41, 01307 Dresden, Germany

## ARTICLE INFO

## Article history:

Received 22 January 2019

Received in revised form 11 June 2019

Accepted 21 June 2019

Available online 27 June 2019

## Keywords:

Stingray

Tesserae

Tessellation

Quantitative backscattered electron imaging

Calcified cartilage

Low-density biomaterials

## ABSTRACT

Skeletal tissues are built and shaped through complex, interacting active and passive processes. These spatial and temporal variabilities make interpreting growth mechanisms from morphology difficult, particularly in bone, where the remodeling process erases and rewrites local structural records of growth throughout life. In contrast to the majority of bony vertebrates, the elasmobranch fishes (sharks, rays, and their relatives) have skeletons made of cartilage, reinforced by an outer layer of mineralized tiles (tesserae), which are believed to grow only by deposition, without remodeling. We exploit this structural permanence, performing the first fine-scale correlation of structure and material properties in an elasmobranch skeleton. Our characterization across an age series of stingray tesserae allows unique insight into the growth processes and mechanical influences shaping the skeleton. Correlated quantitative backscattered electron imaging (qBEI) and nanoindentation measurements show a positive relationship between mineral density and tissue stiffness/hardness. Although tessellated cartilage as a whole (tesserae plus unmineralized cartilage) is considerably less dense than bone, we demonstrate that tesserae have exceptional local material properties, exceeding those of (mammal) bone and calcified cartilage. We show that the finescale ultrastructures recently described in tesserae have characteristic material properties suggesting distinct mechanical roles and that regions of high mineral density/stiffness in tesserae are confined predominantly to regions expected to bear high loads. In particular, tesseral spokes (laminated structures flanking joints) exhibit particularly high mineral densities and tissue material properties, more akin to teeth than bone or calcified cartilage. We conclude that these spokes toughen tesserae and reinforce points of contact between them. These toughening and reinforcing functions are supported by finite element simulations incorporating our material data. The high stresses predicted for spokes, and evidence we provide that new spoke laminae are deposited according to their local mechanical environment, suggest tessellated cartilage is both mutable and responsive, despite lacking remodeling capability.

## Statement of Significance

The study of vertebrate skeletal materials is heavily biased toward mammal bone, despite evidence that bone and cartilage are extremely diverse. We broaden the perspective on vertebrate skeleton materials and evolution in an investigation of stingray tessellated cartilage, a curious type of unmineralized cartilage with a shell of mineralized tiles (tesserae). Combining high-resolution imaging and material testing,

\* Corresponding author.

E-mail address: [mason.dean@mpikg.mpg.de](mailto:mason.dean@mpikg.mpg.de) (M.N. Dean).

<sup>1</sup> Equal contribution (co-first authorship).

<sup>2</sup> Current address: Department of Mechanical Engineering, Virginia Tech, 635 Prices Fork Road, Blacksburg, VA 24060, USA.

we demonstrate that tesserae have impressive local material properties for a vertebrate skeletal tissue, arguing for unique tissue organization relative to mammalian calcified cartilage and bone. Incorporating our materials data into mechanical models, we show that finescale material arrangements allow this cartilage to act as a functional and responsive alternative to bone, despite lacking bone's ability to remodel. These results are relevant to a diversity of researchers, from skeletal, developmental, and evolutionary biologists, to materials scientists interested in high-performance, low-density composites.

© 2019 Acta Materialia Inc. Published by Elsevier Ltd. All rights reserved.

## 1. Introduction

Many hard biological tissues are constructed from self-similar, repeating building blocks, such as scales, plates, or other geometric units. The hierarchical organizations of these building blocks in natural mineralized tissues make them particularly amenable to modeling investigations aimed at characterizing the effects of structure on emergent mechanics at larger scales. However, despite biological materials being composites and therefore intrinsically heterogeneous at all hierarchical levels [1–3], computational mechanical models simulating the mechanical behaviour of biological materials often assume uniform and isotropic properties of the constituent building blocks (e.g. [4–7]). As a result, the roles of “within-building block” structural and mechanical heterogeneities in tissue-level mechanics are often unaddressed, although they may have profound influence on tissue failure properties [8].

The skeletons of elasmobranch fishes (sharks, rays, and their relatives) exhibit a distinct structural tiling, where the uncalcified core of the skeleton is covered in a crust of discrete mineralized tiles called tesserae, typically hundreds of microns wide and thick (Fig. 1). Recent work has shown that individual tesserae are not homogeneous tiles, but rather exhibit complex, three-dimensional patterns of mineral density variation, with implications for both growth pathways and mechanical behavior [9,11]. The concentric Liesegang line banding in tesserae (Fig. 1F), for instance, likely represents successive mineral accretion events responsible for widening and thickening tesserae as animals grow [9,12]. As animals age and tesserae grow wider and come into contact, hypermineralized ‘spokes’ form (Fig. 1E–H). Spokes are acellular, lamellated structures extending from the center region of tesserae to their margins, likely to structurally reinforce the contact points between adjacent tesserae [9]. In contrast, the ‘inter-spoke’ regions intervening between spokes and not associated with joints, are rich with cells (housed in lacunar spaces) and have lower mineral density (Fig. 1E, G). The association of spokes with intertesseral joints, their convergence on the center of tesserae, and the oscillation of their mineral density from lamina to lamina suggest spokes exhibit finescale anisotropic mechanical behavior. Furthermore, in older animals, some of the cell spaces (lacunae) that house chondrocytes in centers of tesserae become ‘micropetrotic’ (filled with a material of high mineral density; Fig. 1H). Yet it is unclear whether this is a cause or effect of the death of the associated chondrocytes and whether this has mechanical implications for stress distributions in tesserae [9,11]. As tesserae are thought to be incapable of repair or removal of mineralized tissue [9,10,13–15], these structural features offer a window into the basic growth processes of the skeleton and how mechanical integrity can be maintained in a growing tissue with no remodeling ability.

In this work, we use a combination of quantitative backscattered electron imaging (qBEI) and instrumented nanoindentation (NI) to investigate the structural-mechanical property relationship in tesserae tissue (i.e. at the sub-building block level). We link structural and mechanical information to growth through

examination of an age series of tesserae from Haller's round stingray, *Urobatis halleri*, the model species for most recent data on tesserae growth and structure. The mechanical properties of tessellated cartilage have previously been studied both theoretically and empirically across a wide range of length scales (e.g. [17–21]). However, the values for material properties reported have varied wildly, from approximately one hundred megapascals to several gigapascals for Young's modulus ( $\sim 1$ –20% of human Haversian bone stiffness; [22]), suggesting unappreciated regional variation and anisotropy of mechanical performance. To address these apparent inconsistencies, we examine mineral density and material properties as a function of animal age, ultrastructural feature, and sectioning plane to begin to understand the relevant axes of variation in this system, to help frame future investigations and sample preparation methodologies. We further incorporate our ultrastructural and material-level mechanical data into finite element analysis (FEA) models to establish a coherence between observed intratesseral features, global tessellation behavior, and the stress fields that evolve within tesserae during loading. These data define key design features of tesserae, providing estimates of their mechanical behavior and baseline inputs for future mechanical models of tessellated cartilage at more macroscopic levels and for biomimetic models of structured tiled arrays.

## 2. Materials and methods

### 2.1. Samples

Tesserae from *Urobatis halleri* were investigated to allow comparison with existing high-resolution data on *U. halleri* skeletal development and tesseral morphology [9,10,12,23–25]. Specimens were donated from another study [26], collected by beach seine from collection sites in San Diego and Seal Beach, California, USA. Ontogenetic stages of the *U. halleri* specimens were inferred based on the width of the animal's body disc (DW), as in previous work [27]. Specimens included in this study were estimated to be: one late-stage (histotroph) embryo (6.0 cm DW), three sub-adults (8.5, 11.0 and 14.0 cm DW) and three adults (19.0, 20.0 and 21.4 cm DW). Yolk sac embryos (DW < 6.0 cm) were excluded, as the first appearance of tesserae was previously reported for *U. halleri* with  $\sim 6.0$  cm DW [9,12]. Animals were shipped on dry ice and stored in a freezer at  $-20$  °C until sample preparation. Specimens were re-thawed in plastic bags in lukewarm water and their skeletal elements (pectoral bar cartilages) were carefully removed and immediately processed for embedding.

Pectoral bars were bisected longitudinally, comparatively flat regions were excised and trimmed down to tessellated strips ( $\sim 0.5 \times 1.5$  cm) with little uncalcified cartilage backing. This sample preparation technique ensured that tessellated strips from different animal specimens came from comparable regions of the skeleton and that each tessellated strip, being from a flat region of the skeleton, contained tesserae of roughly similar size and shape [9,28]. The isolated tesseral layer was air-dried between two Teflon plates, which kept the tesseral layer flat while

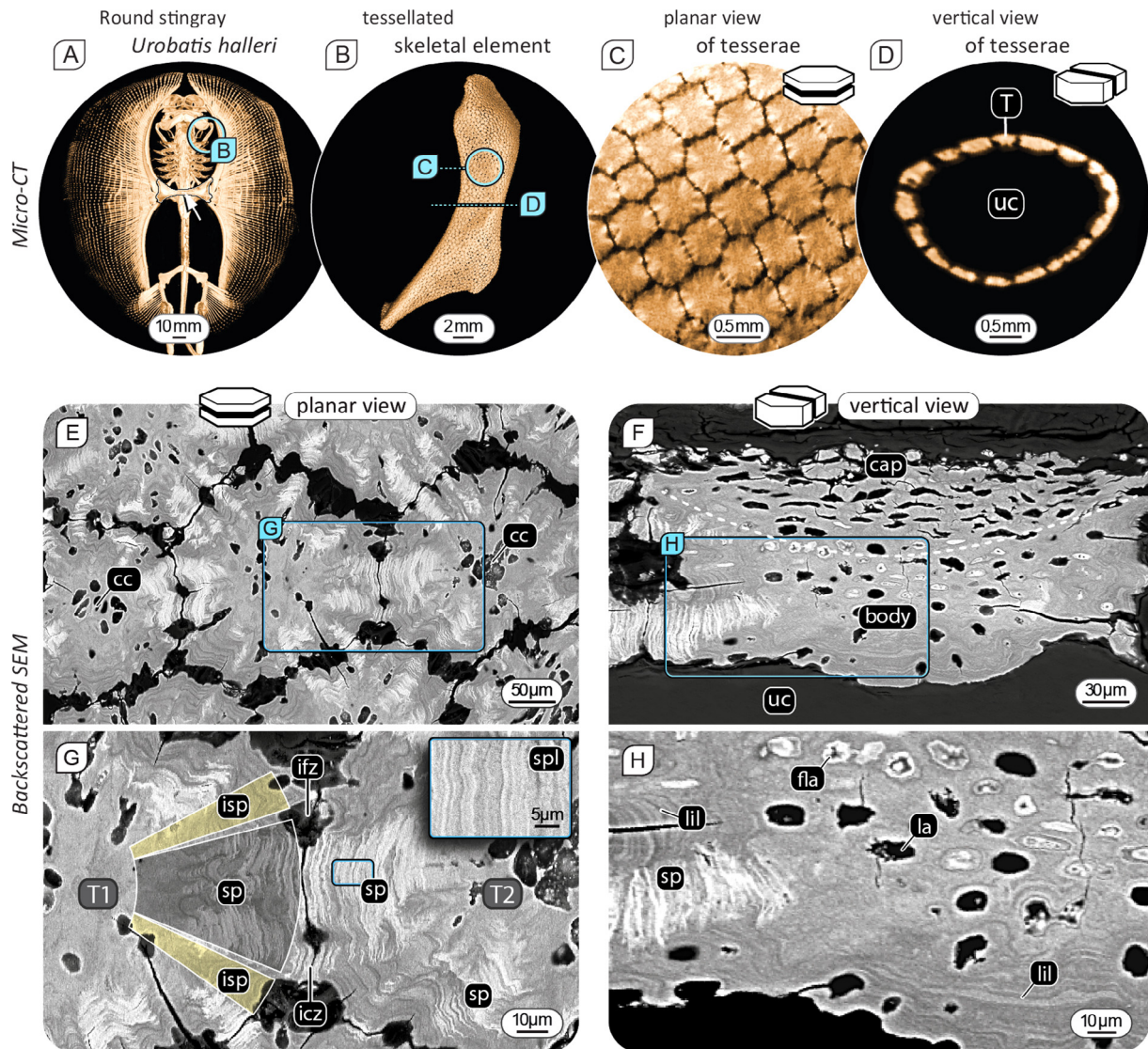


**Fig. 1.** Tesselated cartilage in the skeletons of elasmobranch fish (sharks, rays and relatives). (A–D) Micro-computed tomography (CT) of the skeleton of the study species (Haller's stingray, *Urobatis halleri*). (B–D) Skeletal elements (like the hyomandibula shown in B) are comprised of a core of unmineralized cartilage (uc) covered in a thin layer of geometric, mineralized tiles called tesserae (T). In this study we sampled tesserae from the pectoral bar (white arrow in A). (E–H) The composite arrangement of mineralized and unmineralized tissue in tessellated cartilage is evident in backscattered scanning electron microscope (BSE) images, where tesserae exhibit higher (brighter) backscattered signal intensity and the unmineralized tissues exhibit a comparatively lower (darker) signal (for example the unmineralized matrix and cells housed in intratesseral lacunae; la). Because of their thickened plate-like architecture, individual tesserae in *U. halleri* appear as (E) non-uniform, geometric tiles in 'planar' sections, and (F) roughly rectangular in 'vertical' cross-sections (this sectioning terminology is used throughout the current study). The dashed line indicates the border between the cap and body zones within *U. halleri* tesserae. (G–H) In higher magnification images of (G) planar and (H) vertical sections of individual tesserae from adults, a high degree of local variation of mineral density is visible, associated with specific structural features: lacunar spaces housing unmineralized matrix and cells (la) or filled (fla) with densely mineralized material; Liesegang lines of varying mineral density parallel to tesseral mineralization fronts (lil) strictly found in the body zone of tesserae; and lamellated, highly-mineralized "spokes" (sp) comprised of spoke laminae (spl) of oscillating mineral density (inset). (G) Spokes are associated with points of contact between abutting tesserae (iccz = intertesseral contact zone), whereas Liesegang lines are visible in interspoke regions (isp) flanking zones of fibrous connection between tesserae (ifz = intertesseral fibrous zone), appearing as dark gaps in BSE. (E–G: animal disk width [DW] = 19 cm, F–H: DW = 21.4 cm). Images modified from [9,10].

preventing sticking during drying. Dried samples were cut into smaller pieces and placed in a custom-built poly-methyl methacrylate (PMMA) holder, according to the desired sectioning orientation (vertical or planar sections; see below). Since tesserae are typically six-sided [28] and wider than they are thick, they are roughly hexagonal when sectioned in the plane of the tesseral mat (planar sections) and rectangular in transverse cross-sections of skeletal elements (vertical sections) (Fig. 1). Samples were embedded in PMMA, cut in slices ( $300 \pm 100 \mu\text{m}$  thick; Buehler Iso-Met low speed saw) and mounted on a PMMA object slide using double-faced adhesive tape. Sections were polished with alu-

minium oxide pads with descending grain size (Logitech PM5 Precision Lapping and Polishing Machine), and then with a soft polishing plate with an aerosol diamond suspension ( $0.25 \mu\text{m}$  grain size).

*Urobatis* tesserae are, depending on animal age,  $<500 \mu\text{m}$  in any linear dimension and exhibit complex ultrastructural arrangements [9,10,12], making it very difficult to target specific structures in sectioning. The central region of tesserae, for example, is only  $\sim 30 \mu\text{m}$  in each linear dimension [9]. Our sample preparation technique, however, offered a *post hoc* method for locating specific regions, in allowing sections of prescribed orientation (vertical or

planar) through relatively planar tessellated layers containing tens of tesseræ. This ensured that each section contained multiple tesseræ, although the sectioning plane passed through each in a slightly different anatomical plane. Tesseræ are structurally heterogeneous, but often largely rotationally symmetrical about their centers in planar sections (Fig. 1). Through light and electron microscopy examination of sections from both sectioning orientations (vertical, planar), we used the distinct cell lacunae distribution patterns in tesseræ as anatomical guides (Fig. 1) (see [9]), locating individual tesseræ that had been sectioned approximately through their center regions. These tesseræ were then used for subsequent qBEI and nanoindentation experiments (see below). Examinations of whole sections also allowed us to observe general aspects of morphology, and to compare these with results of previous studies (e.g. [9,12]).

As only cutting planes through the central regions of tesseræ were considered comparable, sample sizes for each ontogenetic stage varied due to the availability of appropriately-sectioned tesseræ (Table S1). Only vertical sections were analysed for specimens  $\leq 11.0$  cm DW, as tesseræ were too thin for accurate planar sections; for all other specimens, both vertical and planar sections were prepared. Having both planar and vertical sections allowed comparison of mineral density variation and mechanical anisotropy in the two orientations.

## 2.2. Quantitative backscattered electron imaging (qBEI)

### 2.2.1. Experimental design

Quantitative backscattered electron imaging (qBEI) was performed on the polished and carbon coated sample blocks to determine the local calcium (Ca) content of the mineralized tissue. Previous energy dispersive spectroscopy (EDS) analyses of tesseræ have demonstrated that grayscale variation observed in BSEM can be attributed purely to changes in mineral density and not elemental composition [9]. We used a field emission scanning electron microscope (FE-SEM, Supra40 Zeiss, Oberkochen) operated in the backscattered electron mode with 20 keV acceleration voltage at 10 mm working distance, generating a specimen current of approximately 300 pA. As the intensity of backscattered electrons is proportional to the average atomic number of queried regions on the sample surface, after the calibration routine, the local Ca concentration of the sample can be calculated based on the local gray values in the images. We used carbon ( $Z = 6$ ) and aluminum ( $Z = 13$ ) calibration standards and set the gray values of these elements to 25 and 225 respectively. Under careful control of the system stability, images of tesseræ were obtained with a pixel resolution of  $0.5 \mu\text{m}$ . qBEI is an established method for the quantification of the Ca concentration in human and animal bone [29,30]; more information on the calibration routine and the validation of this method with energy dispersive X-ray analysis can be found in [31,32].

Previous methodology was optimized for bone rather than mineralized cartilage [32] and so required modification in order to account for the large number of sulfated proteoglycans in cartilage organic matrix. We found the gray value of non-mineralized cartilage ( $28.4 \pm 3.8$ ) to be higher than that of human osteoid ( $25 \pm 2.7$ ; [33]) and used this as the non-mineralized baseline value (0 wt% Ca). Additional calibration conditions were unchanged, resulting in the following relationship for the conversion from gray value to Ca content for tesseræ:

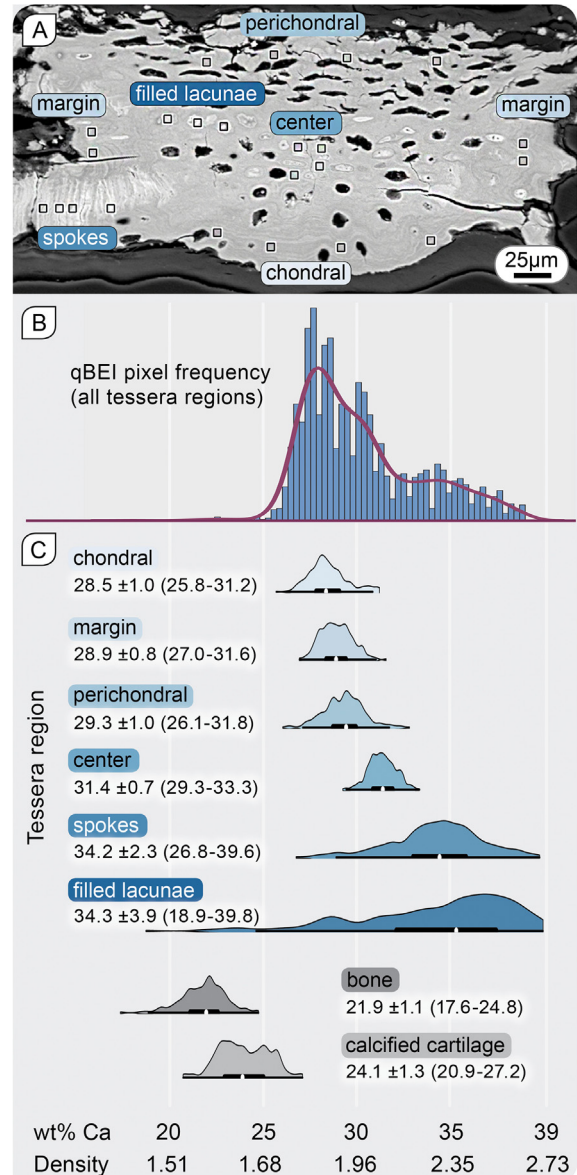
$$\text{wt\% Ca} = 0.1757 * \text{GV} - 4.9894 \quad (1)$$

Image pixels and gray values were converted to microns and wt% Ca, respectively, according to the relationships stated above. All wt% Ca measurements and statistics were performed on original

(unaltered) qBEI images; the brightness and contrast of the BSE images in figures (e.g. Figs. 1–7, 9), however, have been adjusted to enhance structural features of interest (e.g. spokes).

### 2.2.2. Mineral density as a function of age and location/anatomical feature

To examine mineral content as a function of location, the mineral content of specific features were investigated using a custom-built Python script. Selective area analyses were performed on a vertical section of a single adult tessera ( $21.4$  cm DW) in five anatomical regions (center, chondral, perichondral, margin and spokes), sampling four sites of  $4.98 \times 4.98 \mu\text{m}^2$  ( $10 \times 10$ -pixel,  $\sim 25 \mu\text{m}^2$ ) (Fig. 2). Sampling sites 1–4 were pooled (400 pixels =



**Fig. 2.** Characteristic mineral densities of intra-tesseral features in a representative tessera. (A) BSE (non-qBEI) images of a vertical-sectioned tessera ( $21.4$  cm DW). For each of the indicated structures/regions, four regions of interest (ROIs) of  $10 \text{ pixels}^2$  ( $\sim 25 \mu\text{m}^2$ ) each were selected, and gray value/wt% Ca distributions calculated. (B) Mineral density (wt% Ca) frequency distribution for all ROIs in (A). (C) Histograms, average, standard deviation and range of the mineral densities (wt% Ca) for structures/regions in (A), with comparison to human bone and calcified cartilage (Gupta et al., 2005). The conversion of the mineral content (wt% Ca) to tissue density ( $\text{g}/\text{cm}^3$ ) is shown at the bottom. Plot characteristics: thin black line = 95% confidence interval, larger black line = interquartile range (25–75 percentiles), white dot = median. See Supplemental Table 1 for values in tabular format.

$\sim 100 \mu\text{m}^2$ ) yielding the wt% Ca value for each region in the tessera section.

Tesserae are believed to grow by the accretion of mineralized tissue at their margins and therefore tesserae from older animals are larger than those from younger animals [9,12]. As a result, only the central regions of tesserae from different ontogenetic stages are directly comparable, with the margins of tesserae representing the growth fronts (regardless of age). To examine mineral density at different growth stages, we compared the results of selective area analyses from two representative tesserae regions—the center and margin—from one vertical-sectioned tessera for each of the examined ages (Table S1). For the 6 cm DW animal, tesserae were too small to distinguish between center and margin (Fig. 3A).

To validate the above method for investigating mineral content as a function of location, images were processed with a custom macro for Fiji (ImageJ v1.50b, NIH) as follows: (i) thresholding, to separate background and cracks from the mineralized tissue, (ii) erosion of 2 pixels from the margin of the mineralized tissue selection in order to exclude edge effects, (iii) reduction of the resolution to  $2.5 \mu\text{m}$  pixel size to exclude partially filled pixels from the evaluation, (iv) determination of each pixel's gray value and position with respect to the tesseral center (the calculated center of mass of all non-background pixels), (v) exporting the data as a function of an angular vector (azimuthal direction) and linear radial distance. Datasets typically contained large numbers of pixels (between 5000 and 20,000), and so data were visualized by plotting mineral content in point density plots as a function of azimuthal direction or radial distance using SigmaPlot (Fig. 4). This approach illustrated the locational probability of certain mineral densities and so allowed examination of the relationship between mineral content and location within a tessera. The angular vector provided a means of comparison of regions arrayed in different azimuthal directions around the center, allowing comparison of spoke and interspoke regions in planar sections (Fig. 4A) and comparison of perichondral, chondral and lateral (joint-associated) regions in vertical sections. In contrast, the radial distance variable permitted, for example, comparison of mineral content at tesseral centers (distance = 0) and margins (distance = maximum) (Fig. 4B).

### 2.2.3. Spoke mineral content and periodicity

We performed an initial examination of the organization of spokes from a subset of 19 'spoke-pairs' (spokes from adjacent tesserae, abutting at contact zones; Fig. 5, Table S1) from planar sections of tesserae from three individuals (14.0, 19.0 and 20.0 cm DW). Intertesseral contact regions were chosen with prominent spokes. Spoke-pair images were rotated so that the laminae and the joint space were vertical in the image and then cropped to include spoke regions of roughly similar size from the tesserae on the left and right sides of the joint space ( $\sim 5 \mu\text{m}$  tall  $\times$  20–40  $\mu\text{m}$  wide). By performing these cropping and reorienting steps, the spoke laminae were largely parallel and vertically-oriented. Cropped images were analyzed with a custom MATLAB script, plotting for each row of pixels in an image the mineral content vs. distance from the joint space, coaligning all curves at their first mineral content peak (the local maximum closest to the joint space). The script averaged all generated by-row linescans to produce average plots for mineral content variation as a function of distance, for both 'left' and 'right' tesserae. Left and right curves were then coaligned at their first mineral content peaks and visually compared for symmetry. Although spokes and their laminae were clearly visible in qBEI images (e.g. Fig. 1E, H), the field of view required to visualize whole tesserae for other portions of this study precluded examination of the fine ultrastructural details of spokes at their relevant resolutions (e.g. at pixel dimensions of  $<0.5 \mu\text{m}$ ). Our spoke analysis therefore greatly simplifies the actual mineral density variation in spokes, but creates an average linear transect of a small area around the joint, allowing a first approximation of spoke architecture.

### 2.3. Nanoindentation

To probe the correlation between local mineral density and mechanical properties, nanoindentation was performed on the same fine-polished samples that had been previously imaged with qBEI, allowing direct comparison of the mechanical properties and mineral density in specific locations. Similar approaches have been used in the past to map mineral content and mechanical properties

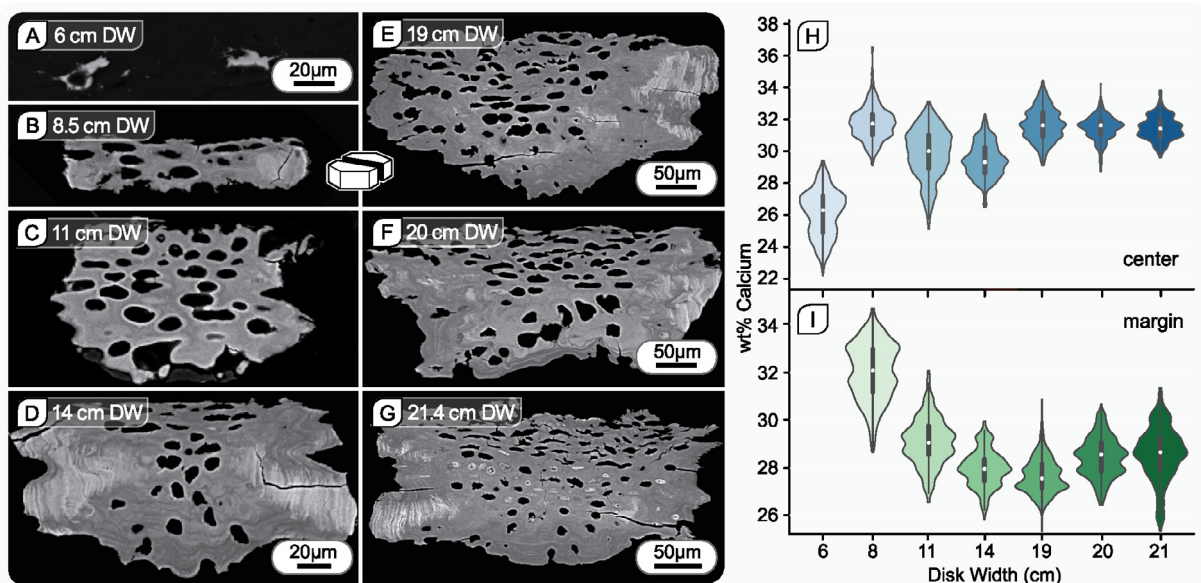


**Fig. 3.** Mineral density variation during tesserae development. (A–G) BSE (non-qBEI) images of vertical sections of representative individual tesserae from an age series of *U. halleri* (ranging from 6 to 21.4 cm DW). Note, adjacent tesserae have been removed from these images. (H–I) Violin plots (mirrored histograms) of mineral density (wt% Ca) as a function of animal age (characterized by DW), for (H) center and (I) margin regions, as indicated in Fig. 2A (plot characteristics as in Fig. 2). Note that the 'margin' is further from the 'center' as animals age (i.e. as tesserae increase in size). Over ontogeny, the center increases in mineral density to a threshold level ( $\sim 31$  wt% Ca), whereas the margin, where new material is deposited, exhibits a consistently lower mineral density (see Fig. 2C). See Supplemental Table 1 for by-age descriptive statistics.

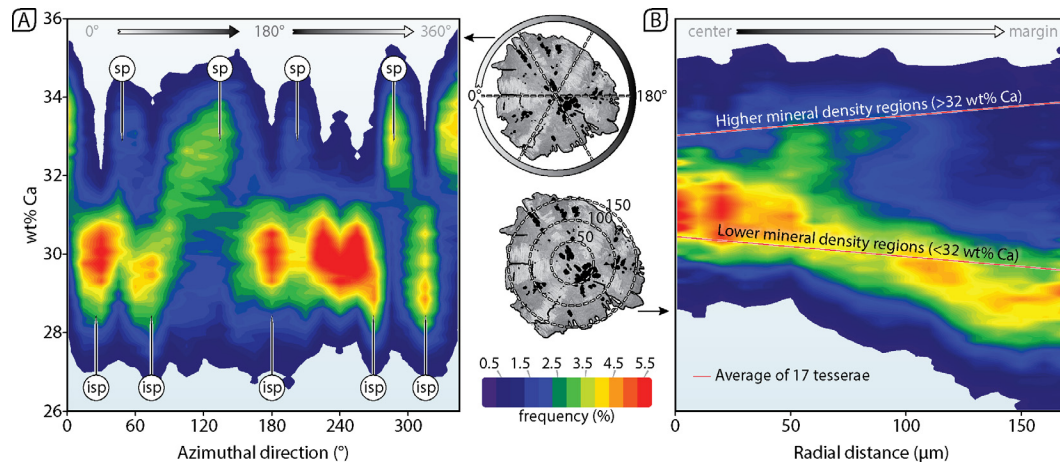


**Fig. 4.** Spatial variation of mineral density within tesserae. Scatter density plots of mineral density (wt% Ca) as a function of (A) azimuthal angle and (B) the radial distance from the center of a single adult tessera (19 cm DW). Tesserae icons (non-qBEI BSE images) in the middle of the figure depict the method of analysis performed in panels A and B, with the color scale representing pixel density/probability (i.e. for a given x-axis value, the probabilities of all y-axis values sum to 1.0 = 100%). (A) In planar sections, the alternating pattern of spoke regions (labeled 'sp') and interspoke regions (labeled 'isp') is evident from the oscillating sequence of higher mineral density and lower mineral density peaks in the angular vector analysis. (B) Spokes (regions  $>32$  wt% Ca) often showed little change in mineral density with distance from the tesseral center. In contrast, non-spoke regions ( $<32$  wt% Ca) showed decreasing mineral density with radial distance. Overlaid red lines indicate the average linear trends for spoke and non-spoke regions for 17 tesserae (9 vertical-sectioned and 8 planar-sectioned tesserae). The trend for non-spoke regions is consistent for tesserae of all ages, indicating that newly-deposited (more peripheral) tissue is typically lower in mineral density. (For interpretation of the references to color in this figure legend, the reader is referred to the web version of this article.)

in human bone and calcified cartilage [34,35]. The mechanical data were first filtered to remove data points within and close to structural defects, such as lacunar pores or other gaps in the tissue. To correlate between high-resolution mineral density (qBEI) and mechanical data (nanoindentation) over cross-sections of whole tesserae, it was necessary to use dehydrated, PMMA-embedded and polished specimens. While dehydration tends to increase the measured indentation modulus and hardness relative to hydrated tissues, the trends we report for mineral-density dependent mechanical properties are likely similar between hydrated and dried states. Additionally, the very high mineral densities we report (see below) argue that most tissue regions are likely to be less susceptible to dehydration artifacts [36,37].

Load-controlled nanoindentation was performed on polished planar and vertical sections using a Berkovich diamond probe tip (trigonal pyramid, semi-angle =  $65.3^\circ$ , radius  $<100$  nm) on a Hysitron TriboIndenter (Bruker Corporation, Billerica, MA, USA). The piezoelectric transducer was first allowed to equilibrate for 105 s (the last 45 s with digital feedback) and another 40 s for calculating drift automatically prior to each indent. Typical load functions included loading (10 s), holding (20 s), and unloading (10 s). The maximum load was 2 mN for nanoindentation mapping measurements. The standard Oliver-Pharr (O-P) methodology was used to quantify the Young's modulus ( $E$ ) and hardness ( $H$ ) of tesseral tissue [38], using the Poisson's ratio (0.07) and Young's modulus (1140 GPa) for the diamond tip and Poisson's ratio commonly used for bone ( $\nu = 0.3$ ; [39]), as the Poisson's ratio of tesserae is unknown. The probe tip area function (the projected area of the indentation tip as a function of the contact depth) and the frame compliance were calibrated prior to each set of experiments using a fused quartz sample.

Representative regions and landmarks were located on samples using an optical microscope installed on the indentation instrument. These landmarks were used to guide the positioning of indentation arrays, with inter-indentation spacing ranging from one to 10  $\mu\text{m}$ . Two sets of experiments were conducted. The first compared mechanical properties of tesserae at different stages of growth, using polished vertical sections from animals at three different ontogenetic stages (DW = 14, 19, and 21.4 cm;  $n =$  one

tessera per age). At younger stages of growth (i.e.  $<14$  cm DW, see Fig. 3), tesserae are small and very porous (i.e. cell lacunae constitute a large proportion of their volume), making it difficult to construct adequate indentation arrays on sample sections. Nanoindentation was performed only in the central regions of the chosen samples (Fig. 6), covering areas of  $87.3 \pm 25.2 \mu\text{m}^2$  ( $331 \pm 97$  indents per sample). Results from preliminary indentation tests performed in smaller regions on other polished samples were consistent with the results reported below for larger indentation arrays.

Second, to investigate regional variation and anisotropic mechanical properties of fully-formed tesserae, indentations were performed on both planar and vertical polished tesserae cross sections from an adult animal (DW = 19 cm;  $n =$  one tessera per orientation) (Fig. 7). The indentation arrays extended from the center of the tessera to its lateral edge, including the spoke regions at the intertesseral joint, covering an area of approximately  $16,819 \mu\text{m}^2$  for the planar section ( $130 \times 130 \mu\text{m}$  array; 2800 indents) and  $14,400 \mu\text{m}^2$  for the vertical section ( $120 \times 120 \mu\text{m}$  array; 961 indents).

To correlate mineral density (from qBEI data) with mechanical properties (from instrumented nanoindentation), qBEI images were first manually aligned with the indentation arrays using corresponding optical images. After alignment, the qBEI images (pixel size =  $0.5 \mu\text{m}$ ) were downsampled to match the larger spacing of nanoindentation arrays ( $\sim 2 \mu\text{m}$ ). In this way, mineral density (qBEI) and modulus/hardness (nanoindentation) could be correlated on a by-pixel basis. The image downsampling method is discussed in Fig. S1.

#### 2.4. Statistical methods

Descriptive statistics (e.g. data range, mean, median, standard deviation) were tabulated for all data distributions resulting from qBEI and nanoindentation experiments (Figs. 2 and 3; Table S2). Locally weighted scatterplot smoothing (LOWESS) trendlines from the Matplotlib library [40] were used to help visualize relationships between mineral content and distance from the tesseral center (Fig. 4). The connections between disc width (maturity stage) and tesseral mineral content were explored by plotting wt%

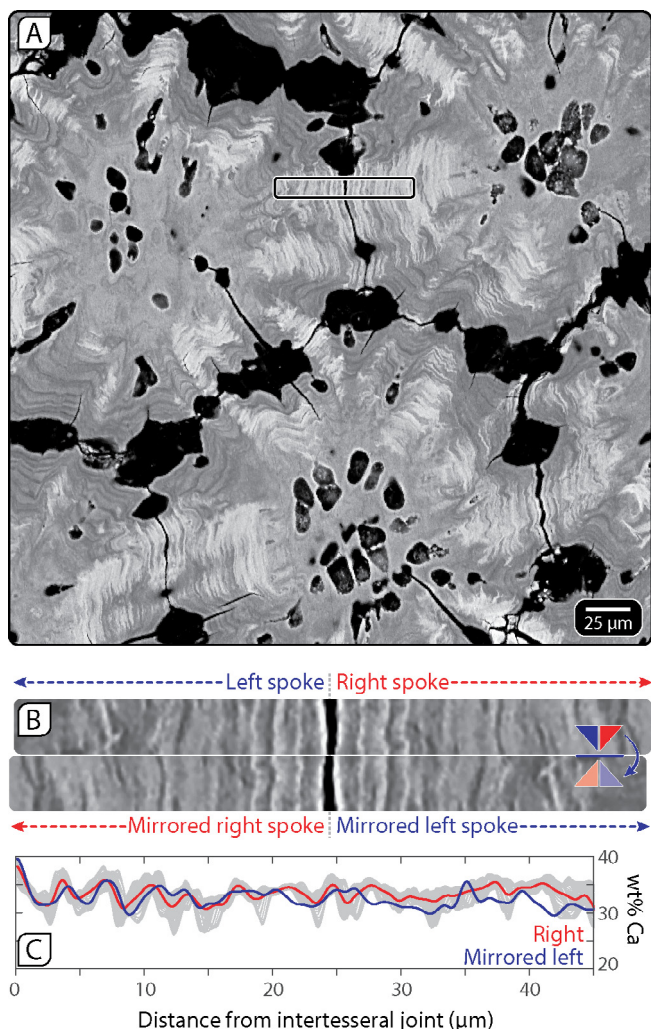


**Fig. 5.** Oscillating mineral density and pattern correspondence of spoke laminae. (A) BSE (non-qBEI) image of a planar section of several abutting tesserae, showing the high-mineral density, lamellated pattern of spokes associated with intertesseral joints. Spoke laminae are predominantly parallel to the tesseral edge at the intertesseral contact zone and are believed to represent former surfaces of contact between tesserae. (B) In abutting tesserae, laminae an equal distance from the shared contact region often show remarkable similarity of pattern: the bottom image is a copy of the top image (the boxed region in A), mirrored and flipped horizontally, to illustrate the correspondence between right and left spokes in this image. (C) Average line scans of mineral density (wt% Ca) as a function of distance from the intertesseral joint, overlaid for left and right spokes and aligned by the first mineral density peak adjacent to the tesseral edge. Oscillation patterns for more recent laminae (closer to the contact surface) mirror each other more closely. Gray lines are individual linescans for the right spoke, red and blue lines are linescan averages for the right and left spokes, respectively. (For interpretation of the references to color in this figure legend, the reader is referred to the web version of this article.)

Ca frequency distributions (e.g. Fig. S2) for each examined tessera ( $n = 18$ ; Table S1). The distributions were fit and deconvoluted into a high and low mineral density peak (see Results) using an interactive peak-fitting function in MATLAB [36] and the mean and standard deviation of each peak position were calculated. In the mineral density analysis of spokes, mineral content peaks were located using the *findpeaks* function in MATLAB and used to calculate mineral content maxima, minima and periodicity (a proxy for lamina width) for the averaged curves (Fig. 5). The values for inter-peak distance and all mineral content peaks/troughs were pooled for all spoke images ( $n = 19$ , ~15–25 peaks per tessera per dataset)

and the mean and standard deviation calculated, as well as the absolute maximum and minimum mineral densities observed across all datasets.

Linear modeling approaches were used to quantitatively assess perceived trends in the data and to answer specific questions of interest. To compare mineral densities among regions in an adult tessera (21.4 cm DW; Fig. 2), confidence intervals were calculated around mean percent weight of calcium estimates from each tesserae region (center, chondral, perichondral, margin, spokes, filled lacunae) to evaluate precision, and a Levene's test was conducted to evaluate equality of variances. A one-way ANOVA with Tukey's HSD post hoc test then was used to determine if average mineral density differed significantly among tesserae regions and to pinpoint specific pairwise regional density differences. To explain the relationship between center regions and margin regions throughout ontogeny (Fig. 3), different curvilinear fits were attempted. Multiple regression was used to evaluate the relationship between mineral density (wt% Ca) and material properties (hardness, modulus) across a size range (DW = 14.0, 19.0, 21.4 cm) (Fig. 6). A multiple regression approach also was used to determine if the relationship between mineral density and material properties differed based on sectioning orientation (vertical, planar), presence (>32% wt Ca) or absence (<32% wt Ca) of spokes, and a combination of these factors (Figs. 7 and 8). For all comparisons an alpha value of <0.05 was used to indicate significance of test statistics.

## 2.5. Finite element analysis

In order to relate the observed local mineral density and material property heterogeneities to global mechanical properties in adult *U. halleri* tesserae, a 2D tesserae assembly was modeled using commercial Finite Element software (ABAQUS/Standard), incorporating structural, geometric and mechanical data from tesserae from the current work and previous studies [9,11,41].

A comparison of the qBEI images of the biological tissue in Fig. 9A–C and our abstracted model is shown in Fig. 9D–F. Our simulated tesserae were approximated as hexagonal tiles, since it is common for tesserae to have six sides/neighbors [28]. Tiles were modeled with internal radiations mimicking spokes, semicircular cut-outs at tesseral vertices to mimic pores, and cut-outs in the middle of each side to represent the concave regions filled with fibrous material in the biological tessellation (Fig. 9F) [9,11]. This geometry resulted in the modeled tessera having ~40% of its perimeter in contact with adjacent tesserae. This is in keeping with structural analyses in the current study and a previous examination of tesserae ultrastructure [9], which showed no soft connecting tissue (fibrous material) between tesserae at contact regions. To efficiently model the effects of a larger tiled array (Fig. 9D) and connections between tesserae, we considered a small modeled subunit (representative volume element, RVE) that could be repeated to capture the behavior of an infinite tiling. The rectangular RVE (Fig. 9H; see below) contained two complete tesserae (to capture the interaction effects of two tesserae under compression) and several partial neighbors (RVE height = 519.6 μm) that, when tiled, would create a hexagonal array. Periodic boundary conditions (PBCs) were applied to the top, bottom, left and right sides of the array.

Three distinct regions in the tesserae model – representing spoke, non-spoke regions, and joints – were assigned different material properties, in order to approximate the composite nature of the system. Spoke and non-spoke regions were modeled as linear, isotropic elastic materials with Young's moduli of  $E_S = 30$  GPa and  $E_{NS} = 20$  GPa, respectively (based on data from the current study) and a Poisson's ratio of  $\nu = 0.3$ . Joint regions were assigned

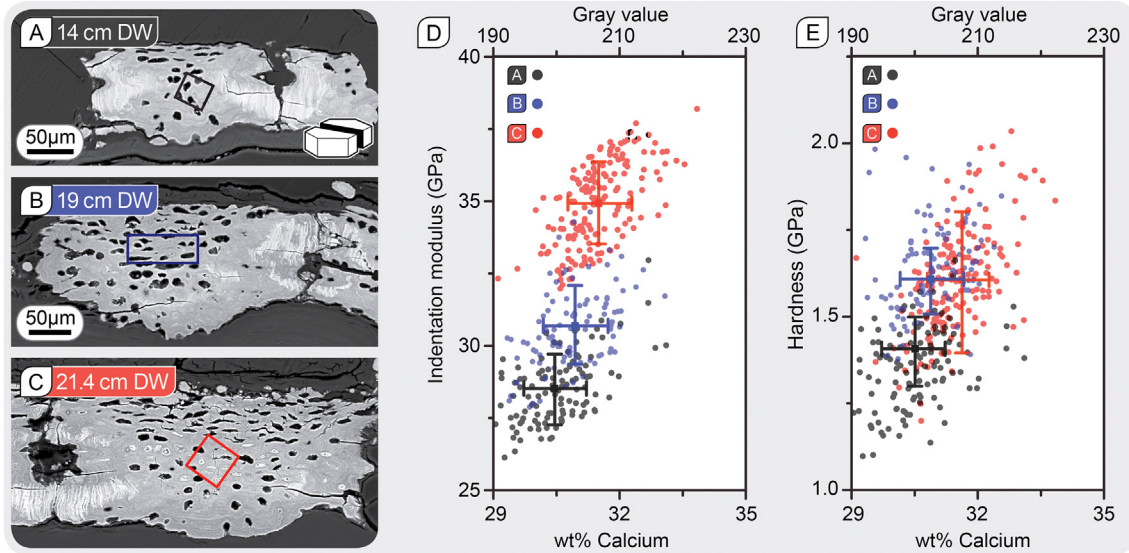


**Fig. 6.** Mineral density and material property correlation of the tesseral center during development. (A–C) BSE (non-qBEI) images of vertically cross-sectioned tesseræ at three different growth stages, indicated by their disc width (DW). The rectangular boxes in the central regions indicate the ROIs for indentation measurements. (D) indentation modulus and (E) hardness as a function of gray value and wt% calcium for the three tesseral center ROIs shown in (A–C). Crosses indicate the average and standard deviation of each tessera. The material properties correlate positively with wt% calcium content, but with indentation modulus increasing more rapidly than hardness with age.

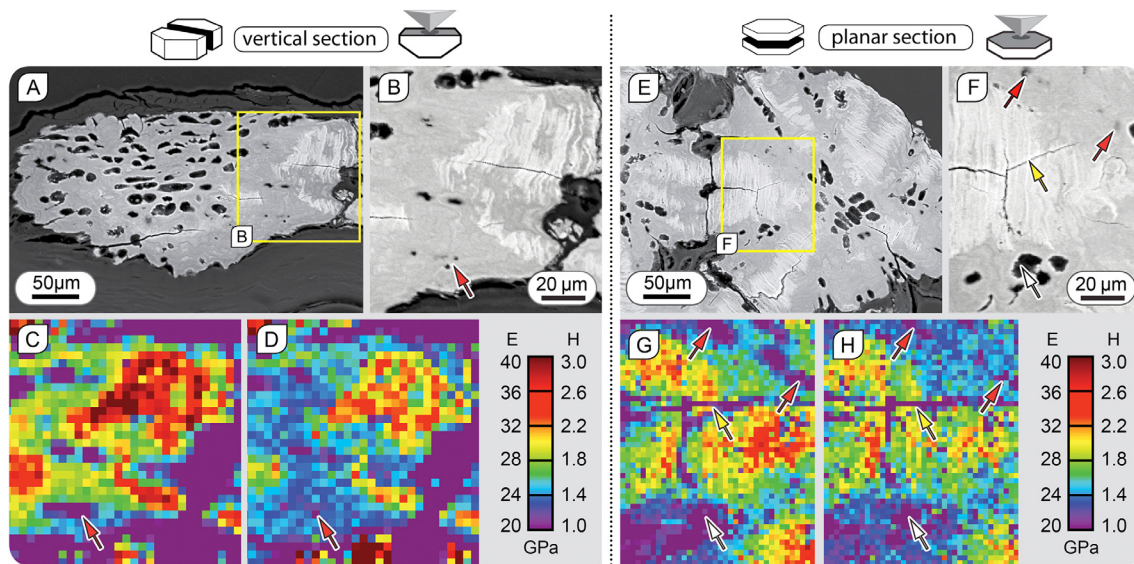


**Fig. 7.** Nanoindentation-derived micromechanical properties of tesseræ in different section planes. (A–B) BSE (non-qBEI) image of a vertical section of a representative tessera; indentation region (yellow box) magnified in (B). Corresponding (C) indentation modulus,  $E$ , and (D) hardness,  $H$ , maps of the same area shown in (B). (E) BSE (non-qBEI) image of a planar section of a representative tessera; indentation region (yellow box) magnified in (F). Corresponding (G) indentation modulus,  $E$ , and (H) hardness,  $H$ , maps of the same area shown in (F). Spokes show significantly higher indentation moduli compared to other tesseral regions in both vertical and planar sections. Arrows indicate structural defects (red arrows = subsurface lacunae, yellow arrow = crack) or natural openings in the sample surface (white arrow = lacunar space). (For interpretation of the references to color in this figure legend, the reader is referred to the web version of this article.)

orientation-dependent material properties, as these areas are filled with linearly arrayed collagen in the biological system. The joint fibers are hypothesized to be considerably stiffer in tension than compression [9,42,43], which should result in different elastic behavior of this tessellated structure under uniaxial compression and tension. For joints, we used the user subroutine UMAT to implement the bimodular material with a tensile Young's modulus of  $E_{j-t} = 0.6$  GPa (similar to that of tendon; [41]) and a negligible compressive Young's modulus ( $E_{j-c} = 0$  GPa). Contact regions between tesseræ were modeled as frictionless interfaces, which

can pull apart under tension (Fig. 9H) and come into contact under compression, following collapse of the narrow ( $0.5 \mu\text{m}$ ) joint gap between tesseræ (Fig. 9I).

We simulated tension and compression within the plane of the tesseral mat using a prescribed displacement loading along the  $y$ -direction (i.e. in the vertical direction in the Fig. 9). Displacement and force loading are equivalent in this study. The *in vivo* loads experienced by tesseræ are not known and displacement is easier to apply and more controllable in the simulation. Simulations were stopped at a maximum compressive strain of 1.25% and tensile

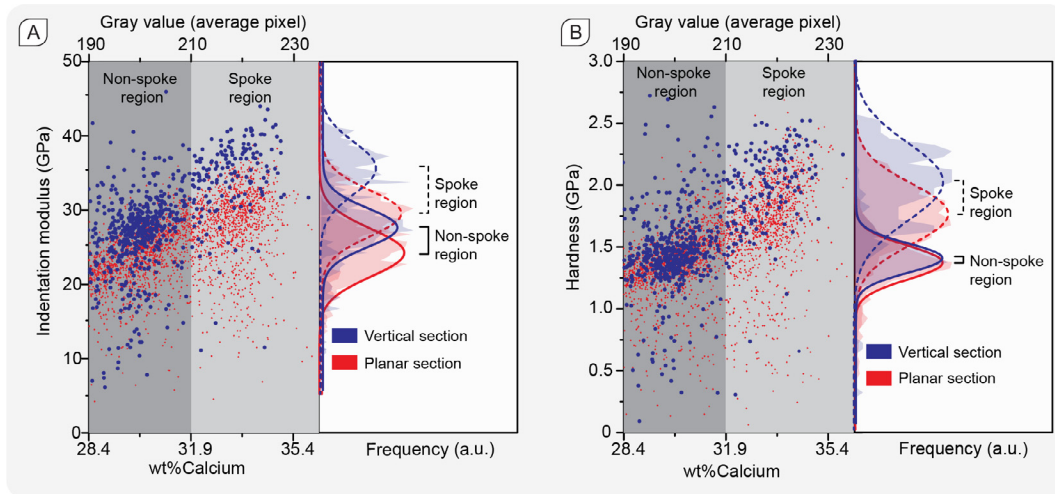


**Fig. 8.** Effects of orientation and mineral density on tesserae nanomechanical properties. (A) Indentation modulus and (B) hardness as a function of BSE gray value and mineral density (wt% Ca) for both vertical and planar cross-sections (blue and red data, respectively). A BSE gray value of 210, corresponding to wt% calcium of  $\sim 32$ , was selected to differentiate spoke and non-spoke region (light and dark gray background, respectively). Frequency distributions and Gaussian fits of indentation modulus and hardness data are shown in the right panels of (A) and (B), respectively, for spoke (dashed line) and non-spoke (solid line) regions. In both sectioning planes, spokes exhibit higher material properties (indentation modulus and hardness) in comparison to non-spoke regions. Tesserar tissue is both stiffer and harder in vertical sections; indentation modulus, however, showed a greater overall degree of anisotropy than hardness (i.e. difference between vertical and planar Gaussian peak positions). Spoke regions showed a larger degree of anisotropy of material properties than non-spoke regions, for both indentation modulus and hardness. (For interpretation of the references to color in this figure legend, the reader is referred to the web version of this article.)

strain of 1.73%, corresponding to applied displacements of 6.5  $\mu\text{m}$  and 9  $\mu\text{m}$ , respectively. These maximum strain/displacement limits corresponded to when the tesserae came into contact under compression and when joint elements began to distort excessively in tension.

### 3. Results

#### 3.1. Quantitative backscattered electron imaging (qBEI)

##### 3.1.1. General changes in structure across ontogeny

Our ultrastructural observations in *U. halleri* tesserae samples during sample preparation and experiments were consistent with previous works [9,12]. Tesserae in older animals were both wider and thicker (Figs. 2 and 3). In late-stage (histotroph) embryos (DW:  $\sim 6$  cm), tesserae were isolated mineral globules within the unmineralized cartilage,  $\sim 20$ – $50$   $\mu\text{m}$  wide and separated from one another by  $\sim 50$   $\mu\text{m}$  gaps (unmineralized cartilage) (Fig. 3A). The typically-described adult tesseral morphology (i.e. polygonal blocks of mineralized tissue) first appeared at disc widths  $\geq 8.5$  cm (young sub-adult stage). At this disc width, each individual tessera exhibited uniformly distributed cell lacunae (ovoid gaps in the mineralized tissue housing cells and unmineralized cartilage; [9,11]). Tesserae continued to increase in size with age, eventually coming into contact with one another (in our samples, in the 8.5 cm DW samples) and developing wide, flat contact zones. Spokes also first appeared in animals of this disc width, always associated with the points of contact between tesserae (intertesseral contact zones, Figs. 1E and 5) [9]. As a result, this disc width represents the establishment of the clear morphological dichotomy between the spoke regions (which lack cells) and the lacunae-rich interspoke regions that intervene between spokes. In animals older than this (i.e. with larger disc widths), it was more common to see micropetrotic lacunae (lacunae, typically restricted to the central portions of tesserae, filled with material of high mineral density, brighter than the surrounding tesseral tissue in backscattered electron images) [25] (Figs. 1H, 2).

##### 3.1.2. General changes in mineral density across ontogeny

Overall, tesserae exhibited a relatively consistent range of mineral densities (wt% Ca), regardless of ontogenetic stage or vertical/planar sectioning orientation (10th to 90th percentiles: wt% Ca  $28.26 \pm 0.63$  to  $33.38 \pm 0.73$ ). In all examined tesserae, frequency distributions for mineral density exhibited a large lower calcium content peak with a ‘shoulder’ at higher calcium contents (Figs. 2, S2). Distributions were therefore best approximated by two overlapping Gaussian curves ( $r^2 > 0.99$ ), with the two deconvoluted mineral density distributions having primary and secondary peaks at wt% Ca  $29.85 \pm 0.71$  and  $32.57 \pm 1.08$ , respectively.

##### 3.1.3. Mineral density variation among structural features

Individual structural features and regions in tesserae exhibited diagnostic mineral densities, with our selective area analysis (Figs. 2 and 3) and linear radial analysis (Fig. 4) methods providing similar results. In the examined adult tessera (Fig. 2), average mineral densities of perichondral, chondral and margin regions (mean wt% Ca: 28.5–29.3) were significantly lower than those of the other regions ( $F = 87.2$ ,  $P < 0.001$ ; Tukey’s HSD,  $P < 0.05$ ). Spokes (mean wt% Ca: 34.2) and filled lacunae (mean wt% Ca: 34.3) had the greatest average mineral densities (Tukey’s HSD,  $P < 0.05$ ) (Figs. 2–5 and Table S2), the spokes being obvious as periodic peaks in our angular analyses of mineral density (Fig. 4A). The average mineral density of the center region (excluding tissue within  $\sim 1$   $\mu\text{m}$  of lacunae) grouped alone as an intermediate condition (mean wt% Ca: 31.4). As a result, in the examined adult tessera, moving from the center of the tessera to the margin in the interspoke region, the mineral density decreased by  $\sim 13\%$  (Figs. 2, 4).

##### 3.1.4. Mineral density variation in tesserae center and margins across ontogeny

Mineral density (wt% Ca) of both center and margin regions changed with animal size, the mineral density of the center region increasing with ontogeny and the reverse trend being evident for the margin (Fig. 3H, I). The mean mineral density in the tessera center was lowest in the smallest animal (6.0 cm DW: 26.1 wt%

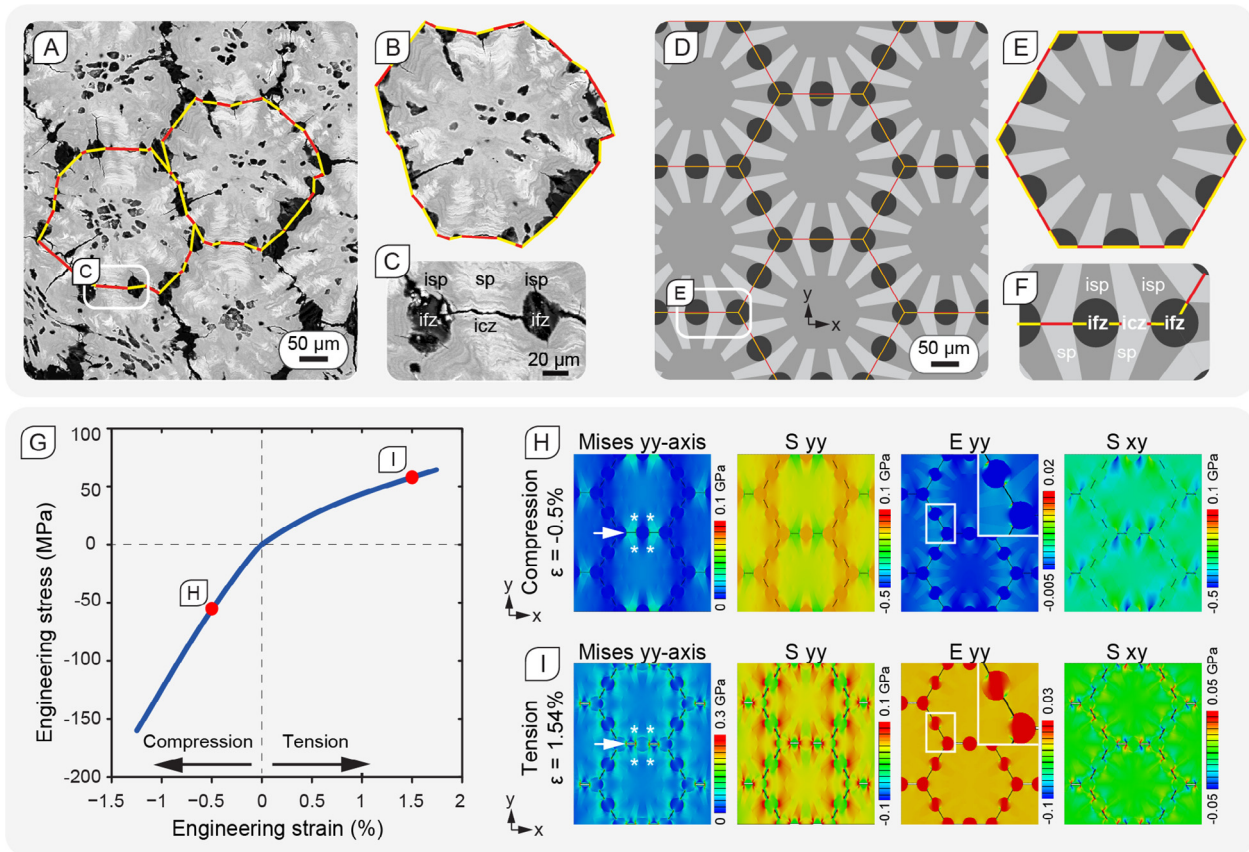


**Fig. 9.** Mechanical properties of a bio-inspired tessellated assembly. (A–C) BSE (non-qBEI) images of increasing magnification of planar-sectioned tesserae, showing heterogeneous mineralization patterns and highly mineralized spokes, with tesserae manually outlined. Red and yellow segments indicate intertesseral contact and fibrous (ifz) zones, respectively. Note the spoke region (t1) flanking the contact zone (icz) and the interspoke region (t2) flanking the fibrous zone (ifz) in (C). (D–F) 2D tesserae models used in FEA simulations, modeled with high and low moduli regions based on nanoindentation data: light (t1 = 30 GPa) and dark gray (t2 = 20 GPa) regions, respectively. Joint material between tesserae modeled as a bimodular material with a tensile modulus of 0.6 GPa, but negligible compressive modulus (0 GPa). (G) Engineering stress–strain curve of the FEA tesserae assembly in tensile and compression loading conditions. Contours of the tesserae assembly in (H) compression at  $\epsilon = -0.5\%$  and (I) tension at  $\epsilon = 1.54\%$ , respectively, for (1) von Mises stress (equivalent stress related to the principal stress, used to predict yielding of material under multi-facial loading conditions), (2) S22 and (3) E22 (normal stress and strain, respectively, along the vertical y-direction) and (4) S12 (shear stress in the x-y plane). White arrows indicate contact zones at intertesseral joints perpendicular to the loading axis, asterisks indicate spokes. Tesserae collide when the model is loaded in compression, but pull apart in tension, causing the asymmetry of the tension–compression slopes in (G). In compression, high stresses occurred in spokes, whereas in tension, high stresses occurred particularly at icz-ifz interfaces (Mises) and high deformation/strain occurred primarily in the fibrous tissue of the joint. (For interpretation of the references to color in this figure legend, the reader is referred to the web version of this article.)

Ca), with larger, older animals exhibiting somewhat variable, but consistently higher mean mineral densities between 29.4 and 31.7 wt% Ca (range: 28.7–34.4 wt% Ca). In contrast, the average mineral density in the margin of tesserae appeared to decrease with animal size from 8.5 to 14 cm DW (from 32.1 to 28 wt% Ca), with all animals with DW  $\geq 14$  cm exhibiting similar mean mineral densities in the margin ( $\sim 28$  wt% Ca) (Table S2).

### 3.1.5. Spoke structural and mineral density variation

Spokes exhibited on average maximum and minimum mineral densities of wt% Ca  $33.4 \pm 1.5$  and  $31.58 \pm 1.9$ , and absolute maximum and minimum mineral densities of wt% Ca 39.21 and 21.21, corresponding respectively to their brighter and darker laminae [9]. Pairs of laminae (consecutive bright-dark layers) were on average  $2.52 \pm 1.0$   $\mu\text{m}$  thick, as determined from the average peak periodicity in line scan analyses. Spokes had complicated gross morphologies, but were typically somewhat triangular in form (in both sectioning orientations), tapering from the intertesseral contact zones toward the tesseral center (e.g. Figs. 1, 3, 5). Within spokes, laminae were often not perfectly straight in cross-section, rather often wavy or crinkled in their morphology (Figs. 1E–H; 5). As a result, capturing corresponding spoke regions from oppos-

ing tesserae was difficult in 2D sections. Regardless, spokes from opposing tesserae often showed impressive degrees of correspondence in their laminar patterns, particularly within 10–20  $\mu\text{m}$  of the contact zone (Fig. 5).

### 3.2. Nanoindentation: mechanical heterogeneity within tesserae

Pairwise comparisons of modeled indentation data indicated that the relationship between material properties and mineral density varied across ontogeny (DW<sub>14.0, 19.0</sub>:  $t = 3.70$ ,  $P < 0.001$ ; DW<sub>14.0, 21.4</sub>:  $t = 4.95$ ,  $P < 0.001$ ; DW<sub>19.0, 21.4</sub>:  $t = -3.13$ ,  $P = 0.002$ ). Modulus was a highly significant explanatory variable for mineral density (wt% Ca) in all three specimens ( $P < 0.001$  for each specimen), with modulus increasing with animal size for any given wt% Ca value (Figs. 6–8). A significant positive relationship between %wt Ca and hardness was additionally found for the largest individual ( $t = 3.48$ ,  $P < 0.001$ ).

The relationship between mineral density and material properties varied by sectioning orientation (vertical or planar) and presence/absence of spokes, with values of modulus/hardness varying nearly two- to three-fold ( $E$ : 20–35 GPa;  $H$ : 1.0–2.5 GPa) and spokes generally exhibiting the highest modulus/hardness

values. An appreciable mechanical anisotropy was observed in tesserae material properties between the two sectioning orientations for both spoke and non-spoke regions (Fig. 8), with indentation modulus/hardness generally higher in the vertical orientation as compared to planar orientation. The indentation moduli of spokes differed the most between the two orientations ( $35.1 \pm 0.2$  and  $29.6 \pm 0.1$  GPa for vertical and planar orientations, respectively). Non-spoke regions exhibited less difference between vertical and planar orientations ( $27.6 \pm 0.1$  and  $24.3 \pm 0.1$  GPa, respectively, Fig. 8A). Similar trends were observed for hardness values, although the differences between sectioning orientations were smaller. For spoke regions, the hardness for vertical and planar orientations were  $2.07 \pm 0.02$  and  $1.77 \pm 0.01$  GPa, respectively. For non-spoke regions, the hardness for vertical and planar orientations were  $1.41 \pm 0.003$  and  $1.37 \pm 0.004$ , respectively (Fig. 8B).

For vertical ( $t = 31.52$ ,  $P < 0.001$ ) and planar ( $t = 73.41$ ,  $P < 0.001$ ) orientations, spoke and non-spoke regions had significantly different relationships between material properties and mineral density. In non-spoke regions in vertical sections, modulus ( $t = 6.59$ ,  $P < 0.001$ ) and hardness ( $t = -2.54$ ,  $P = 0.011$ ) both increased significantly with increasing wt% Ca. In contrast, neither variable was significant in explaining the relationship between material properties and mineral density for vertical regions with spokes (modulus,  $t = 0.84$ ,  $P = 0.401$ ; hardness,  $t = 0.34$ ,  $P = 0.735$ ). In planar sections in regions without spokes, modulus ( $t = 11.94$ ;  $P < 0.001$ ) increased significantly with increasing wt% Ca but no relationship between wt% Ca and hardness was indicated ( $t = 0.72$ ,  $P = 0.470$ ). In contrast, modulus ( $t = -3.47$ ,  $P < 0.001$ ) and hardness ( $t = 7.96$ ,  $P < 0.001$ ) both increased significantly with increasing wt% Ca in planar sections in spoke regions. Significant final models explained a small portion of the overall variability in wt% Ca values ( $r^2 = 0.10$ – $0.20$ ). The relationship between wt% Ca and the combined effects of modulus and hardness differed significantly between spoke ( $t = 5.99$ ,  $P < 0.001$ ) and non-spoke ( $t = -6.73$ ,  $P < 0.001$ ) regions in vertical and planar sectioning orientations.

Both wt% Ca and indentation maps were also useful for identifying structural defects, whether natural (e.g. cell lacunae; Fig. 7F, white arrows) or artificial (e.g. drying cracks; Fig. 7F, yellow arrows), which caused significant variation in wt% Ca or mechanical properties in their proximity (the  $\sim 1$ – $2$  surrounding pixels). In some regions, small pores in qBEI images correlated with much larger zones of lower wt% Ca and mechanical properties (Fig. 7B, F, red arrows). We believe these structural defects to be evidence of cell lacunae lying just beneath the polished surface, resulting in a halo of lower wt% Ca and mechanical properties surrounding the small pore.

### 3.3. Finite element model integration of structure and mechanical properties

The engineering stress-strain curve of the two-dimensional Finite Element model demonstrated a strong tension/compression asymmetry in the mechanical behavior of the tessellated array, where the compressive stiffness ( $\sim 10.5$  GPa) was about three times higher than tensile stiffness ( $\sim 4$  GPa). This asymmetry was a function of the behavior of the intertesseral joint, which opened under tensile loading as stresses were applied to fibers in the joint space (ifz; Fig. 9C, F), but collapsed under compression loading conditions, so that the surfaces of adjacent tesserae (ic; Fig. 9C, F) made contact with each other. This can be observed from the 'closed' and 'open' joint spaces in compression and tension simulations (Fig. 9H-1 and I-1 arrows).

The observed global tension/compression asymmetry and the material heterogeneities in tesserae (derived from our nanoindentation data and incorporated into the model) result in stress

heterogeneities within tesserae that differ with the applied loading condition. Under compression, the spoke regions in line with the loading direction (i.e. where spoke laminae and intertesseral contact surfaces are perpendicular to the loading direction; Fig. 9H-1 asterisks) contribute to the majority of load bearing, whereas the remaining intertesseral contact surfaces and fiber regions (i.e. those not aligned with the loading direction) develop minimal stresses (Fig. 9H-1). In contrast, when the tesserae assembly is under tension, normal stress (S22) and von Mises stress (indicating potential points of failure initiation) are developed radially in tesserae (i.e. not only in regions aligned with the loading direction). These radial stresses are particularly evident in spoke regions, where high stresses can be seen traveling from the fibrous joint spaces toward the center of tesserae via the spokes (Fig. 9I-1). This pattern is a function of the comparatively soft fibrous joints and the diversity of joint contact surface angles relative to the loading direction, both of which allow for sliding displacement of tesserae relative to one another. The relative sliding also leads to the development of local high strains (E22) at the edges of fiber regions in both compression and tension cases, as shown in Fig. 9H-3 and I-3, respectively, although the fiber zone contributes to the majority of total strain in the tension condition (Fig. 9I-3). Furthermore, the relative sliding leads to the development of shear stress at the boundary between mineralized and fiber zones in both loading conditions (Fig. 9H-4 and I-4). However, the stress level in the center of each tessera remained close to zero (Fig. 9H-1 and I-1).

## 4. Discussion

Our analysis of local mineral density and material properties in tesserae allows a first quantitative, tissue-level perspective into the mechanics and growth of elasmobranch tessellated cartilage, and comparison with other vertebrate calcified tissues, such as mammalian mineralized cartilage and bone. Although tesserae exhibit a heterogeneous mineral content ( $\sim 22$ – $40$  wt% Ca), the majority of tissue exhibits a mineral content higher than 27 wt% Ca. In comparison, bone and cartilage are typically below 24 and 27 wt% Ca, respectively (Fig. 2) [35]. This higher degree of mineralization in tesserae is also reflected in the micromechanical properties. The range of values we observed in tesserae (indentation modulus:  $\sim 20$ – $35$  GPa; hardness:  $\sim 1.0$ – $2.0$  GPa) overlaps with the range of values reported for bone and calcified cartilage, yet exceeds the maximum values of those tissues, which attain maximum indentation modulus and hardness of 25 GPa and 1.2 GPa, respectively, for similarly prepared samples [35–37,44,45].

Additionally, our values for stiffness and hardness of dry tesserae are also at least an order of magnitude larger than those reported for both wet- and dry-indentation, non-sectioned shark and ray tesserae examined in other studies [16,18]. Discrepancies between our measurements and those of other studies are surely partly a function of differences in tissue hydration due to sample preparation (see Methods: Nanoindentation above). However, the comparatively high mineral density of the examined tissues suggests they would be less susceptible to the inflations of indentation modulus and hardness that can accompany sample dehydration [36,37]. More importantly, it is likely that the disagreement between our values and those of previous works reflects the variable properties of tessellated cartilage at its different levels of structural hierarchy (e.g. tesserae vs. the composite of tesserae and unmineralized cartilage). For example, indentation measurements by Ferrara and co-authors [18] to characterize white and bull shark tesserae were performed using large conical/conospherical tips ( $100 \mu\text{m}$ ). As an indenter of that size would query a majority of a tessera's material, the reported values likely represent amalgams of the properties of both mineralized and unmineralized tissues

(i.e. mineralized material, but also tesseral joint fibers, and cells and their surrounding unmineralized matrix). This is corroborated by our FEA simulations of the mechanical behaviour of tessellated cartilage at the millimeter scale, which predict that the system's compressive stiffness will be ~30–50% lower than the local stiffness of tesserae, supporting also previous assertions that the soft tissue joints and geometry of tiles (i.e. the arrangement of joints) will contribute significantly to global tissue properties [42,43]. In contrast to Ferrara and co-authors' study [18], our indentation was performed with a Berkovich tip with a far smaller tip radius (~100 nm), with a much shallower indentation depth (typical maximum indentation depth, ~300 nm), on polished sample surfaces, and with ultrastructural features used to guide indentation and avoid non-mineralized tissues. Our data thus represent the first representations of the local (~micron-scale) material properties of mineralized tissue in tessellated cartilage.

Since available evidence indicates that tesserae grow by accretion of new material at their margins [9,12], our investigations of structural feature variation from center to edge provides useful information regarding growth processes in tesserae. For example, our results suggest that non-spoke and spoke regions accrete newly mineralized tissue in different ways during growth. In non-spoke regions (including the center, interspoke, chondral and perichondral areas), newly deposited tissue exhibits comparatively low mineral density that appears to increase with time. This is evidenced by the higher mineral densities of center regions—believed to be the oldest tissue in this non-remodeling/deposition-only system [9]—relative to the mineralization fronts at the tesseral margins (Figs. 2–4). The difference in mineral content between established and newly-deposited tissue is suggestive of a mineralization process similar to bone, where younger osteons are identifiable by their lower mineral densities [46–48].

In contrast, spokes exhibit a relatively consistent range of mineral densities along their lengths, although mineral density oscillates locally from bright to dark spoke laminae (Fig. 5). The factors driving the development of this alternating, laminated pattern remain unclear (but see the mechanistic hypothesis in [9]); our predictions of high stresses at the margins of tesserae (Fig. 9), however, suggest that mechanical factors could play a role in tissue deposition in these regions. The hardness of spokes is >250% higher than values typically obtained for bone prepared under similar conditions and therefore more similar to the hardness of tooth enamel/enameloid [35,44]. High hardness in materials indicates a high resistance to permanent deformation (i.e. a high yield strength; [49]). In tesserae, these very hard features may help reduce the possibility of local material failure in regions of high local stress during skeletal compression. Additionally, *Urobatis* tesserae are anisotropic in their material properties, being on average 13% and 19% stiffer and 3% and 17% harder in vertical than in planar sections (non-spoke and spoke regions, respectively). This anisotropy is not as extreme as the anisotropy of mammalian osteonal bone properties, where axial stiffness may be twice that of orthogonal orientations [50,51]. However, as in bone, anisotropy of tesseral material is suggestive of preferred axes of loading and growth. In particular, the higher stiffness and hardness in the vertical section corresponds to higher mechanical properties within the planar orientation of tesserae, consistent with expected loading conditions for tesserae [19].

Our finite element models indicate that the highest compressive tissue strains mainly reside in the spokes region. This suggests that spokes act as stress sinks, concentrating compressive tissue strains to bear the brunt of contact stress between tesserae, thereby keeping potentially damaging loads from more sensitive tissues (e.g. cells in the interspoke or central regions, Fig. 1; [9]). In this way, spokes likely indicate the primary loading orientations in tesserae, being localized to the regions that should receive the

highest compressive loads from tessera-tessera contact (e.g. when the skeleton is loaded in compression). As all surfaces of tesserae are apparently active growth fronts and therefore modifiable, this would suggest that the in-plane mechanical properties of the tessellation can be continually and locally adjusted, according to changing loading conditions. Such responsiveness is also argued by the variable shape and orientation of individual laminae within a spoke (e.g. Figs. 11, 5 and 7B), which might reflect the variability of a tessera's prior loading regimes. This is underlined by the striking correspondence of laminar pattern between opposing tesserae (Fig. 5), which argues for a shared history of loading between abutting surfaces. Detailed, three-dimensional analyses of these patterns could thus provide deep insight into skeletal loading history and growth.

The comparatively high mineral content and indentation modulus of tesserae suggest that the nanoscale structuring of the tissue may differ in some respects between tesserae and mammalian bone and mineralized cartilage. For example, for human calcified cartilage, values up to 27 wt% Ca are reported, what is distinctly lower than the average values we report for adult tesserae (Fig. 2C) [35]. Furthermore, the average calcium content of whole tesserae (~31 wt% Ca) translates to a tissue mineral content of ~77% dry weight or a mineral volume fraction of ~0.62 (assuming the densities of hydroxyapatite and dry cartilage organic matrix; [35,52]). This mineral content is considerably higher than the mineral volume fractions of mammalian bone and mineralized cartilage, which typically range from 0.35 to 0.40 and rarely exceed 0.50 [35,39]. The differences between elasmobranch and mammalian mineralized tissues are further underlined by examining our results in the context explored by Gupta and co-authors [35], where volume mineral fraction and modulus from human patellar calcified cartilage were compared with mineral crystal aspect ratios ( $\rho$ ) predicted from a staggered model for mineral packing in an organic matrix (Fig. 10). Although the mineral is apatitic in both tesserae and human articular calcified cartilage [24,25,53], tesseral tissue populates a region of the mineral content-modulus graph that is largely unexplored by human articular calcified cartilage, although the model predicts both tesseral and human calcified cartilage crystals to largely exhibit the same aspect ratio ( $\rho = 10$ ). Tesseral crystals may therefore be of the same shape as those of human calcified cartilage, yet a different size or in a different packing arrangement in order to achieve the larger observed mineral density and indentation modulus. Indeed, the only reported data on the crystal size in tesserae suggests that the crystallite domains are smaller and/or more disordered than in (amniote) bone [24]. Tesseral tissue with very high mineral fractions (>0.6) is predicted to comprise crystals of lower aspect ratio, arguing that high mineral content features (e.g. center regions, spokes) may possess distinct crystal structure. The fact that tesseral crystals do not sit perfectly along any one contour in the graph, however, could also mean that the staggered model of organic-mineral interactions is not suitable for tesserae.

The laminar structure and high local indentation modulus and hardness values of spokes point to an efficient design and load-bearing strategy in tessellated cartilage at multiple size scales. The mineral content of tesserae suggests a comparatively high overall tissue density for the mineralized portion of the skeleton (~2.4–2.7 g/cm<sup>3</sup>, calculated assuming that the dry tissue comprises mineral and organics; [52]). However, at a larger size scale, hydrated pieces of shark and ray tessellated cartilage (i.e. including both tesserae and unmineralized cartilage) are considerably less dense (~1.2–1.4 g/cm<sup>3</sup>, reported in [54]; calculated also from [17] using equations in [52] and assuming tissue water density of saltwater, 1.03 g/cm<sup>3</sup>). The low density of the composite tessellated cartilage tissue is surely a function of the very high water content of the unmineralized cartilage [17] and results in the tessellated carti-

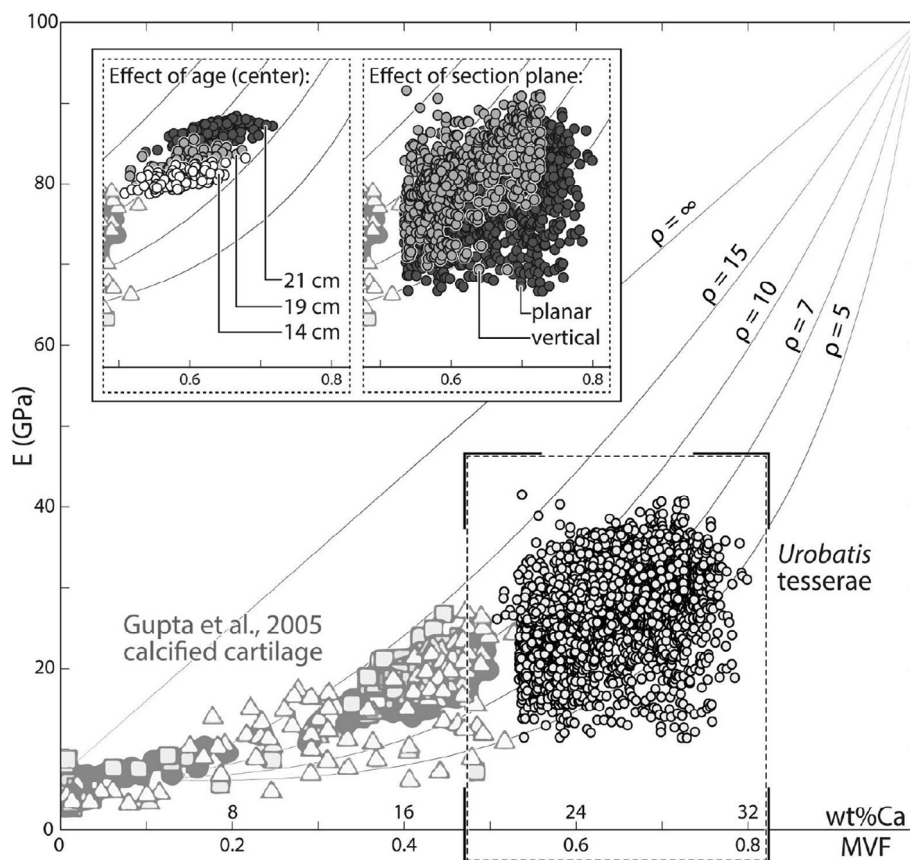


**Fig. 10.** Modulus-mineral relationships of tesseræ and human calcified cartilage. Mineral volume fraction (mvf, converted from wt% Ca; see text) and modulus ( $E$ ) relationships for human patellar calcified cartilage (Gupta et al., 2005) and tesseræ (darker point cloud). The relationship between modulus and mvf is based on a staggered model for mineral packing in an organic matrix, where the mineral crystals are characterized by the crystal aspect ratio ( $\rho$ ). Tesseræ mineral occupies a different region of the mvf- $E$  space, but follows a similar predicted crystal aspect ratio contour line to human calcified cartilage (except, perhaps, at high mvf values). Inset images isolate particular datasets in the tesseræ point cloud, demonstrating the effect of age on the properties of the tesseræ center (left) and the effect of sectioning plane (right). See [Supplemental Table 1](#) for regression data.

lage being approximately 60–75% the density of other, more completely mineralized vertebrate skeletal tissues (e.g. adult mineralized turkey tendon, antler, compact bone, enamel and dentine; [32,54–57]). Mammalian bone tissue, for instance, independent of aquatic or terrestrial habitat, typically exhibits a higher mass density (ca. 1.8–2.0 g/cm<sup>3</sup>) for approximately the same material stiffness as tesseræ (e.g. [31,39,55,57]). Our data therefore argue that tessellated cartilage is particularly mechanically efficient as a vertebrate skeletal tissue, combining low overall tissue density, with high stiffness and high mineral density features occurring only in those regions where stresses should be highest: at a larger size scale, at the peripheries of skeletal elements (where tesseræ are located), and then more locally, at points of contact between tesseræ (where spokes reinforce joints) (this study; [9,42,43]).

Our finite element simulations of bioinspired tesseræ arrays, incorporating ultrastructural features and mechanical properties measured from *Urobatis* tesseræ, capture the asymmetry in tensile and compressive stiffness predicted by previous analytical models (Fig. 7) [42,43]. The difference in tension and compression behavior is largely a function of the way the fibrous joints between tesseræ were modeled, allowing tesseræ to pull apart from one another when the array is loaded in tension, but collide in compression. In this way, under the different loading regimes, the location of the highest stresses shifts to the tissues best able to manage them (the tesseræ in compression and the joint fibers in tension) [42,43]. If this hypothesis is correct, the ability for the intertesseræ joint material to bear large tensile deformations would permit the

tessellation to maintain its structural integrity even under tension; this is in contrast to bone, which is much weaker in tension than compression, making the former a more dangerous loading regime [39,45]. Furthermore, the intertesseræ gaps should effectively suppress defect size if permanent tissue damage does occur, by exhausting a crack's energy in the soft tissue between tesseræ, ensuring that damage remains local rather than jumping between tesseræ. We conclude that, whereas bones of terrestrial animals are preferentially optimized for bearing compressive loads from body weight, the heterogeneous arrangement of soft and hard tissues in tessellated cartilage is optimized for both tension and compression, a successful strategy to avoid damage from loads more relevant in an aquatic environment.

## 5. Conclusions

Our findings provide high-resolution, materials-level perspectives on the growth and structure of shark and ray tessellated cartilage, demonstrating tesseræ to be structurally-complex, while suggesting they are also adaptable architectural subunits. Although similar in composition to other mineralized vertebrate skeletal tissues, tesseræ exhibit mineral densities and tissue stiffnesses/hardnesses that exceed those of bone and mineralized cartilage. This observation argues for a distinct nanoscale tissue organization underlying their predicted high yield strength, in order to prevent damage in the absence of repair mechanisms. We show that in

tesserae, the highest mineral density tissues are employed sparingly and efficiently to manage the highest stresses and protect sensitive tissue compartments (e.g. those occupied by cells) from damaging strains. Our data also suggest that tesseral growth fronts may allow regional tuning of mechanical properties in response to changing local stresses from global loading regimes. These features collectively allow tessellated cartilage to be a high-performing and adjustable skeletal alternative to bone, despite the limitations of its non-remodeling, cartilage base materials.

## Acknowledgements

We thank Kady Lyons for providing samples, Callie Crawford and Paul Zaslansky for CT scans in Fig. 1, Birgit Schonert for sample preparation, and Alan Schwartzman and Zhifei Deng for technical assistance. This study was funded by an HFSP Young Investigators Grant (RGY0067-2013) to MND and JCW; MND was supported by DFG-FR 2190/4-1 Gottfried Wilhelm Leibniz-Preis 2010. LL also acknowledges start-up support from the Department of Mechanical Engineering at Virginia Tech.

## Appendix A. Supplementary data

Supplementary data to this article can be found online at <https://doi.org/10.1016/j.actbio.2019.06.038>.

## References

- [1] G. Mayer, M. Sarikaya, Rigid biological composite materials: Structural examples for biomimetic design, *Exp. Mech.* 42 (2002) 395–403.
- [2] J.W.C. Dunlop, R. Weinkamer, P. Fratzl, Artful interfaces within biological materials, *Mater. Today* 14 (2011) 70–78.
- [3] Y. Shao, H.P. Zhao, X.Q. Feng, H. Gao, Discontinuous crack-bridging model for fracture toughness analysis of nacre, *J. Mech. Phys. Solids* 60 (2012) 1400–1419.
- [4] G.X. Gu, M. Takaffoli, M.J. Buehler, Hierarchically enhanced impact resistance of bioinspired composites, *Adv. Mater.* 29 (2017), <https://doi.org/10.1002/adma.201700060>.
- [5] L.S. Dimas, M.J. Buehler, Tough and stiff composites with simple building blocks, *J. Mater. Res.* 28 (2013) 1295–1303.
- [6] S. Frölich, J.C. Weaver, M.N. Dean, B. Birkedal, Uncovering Nature's design strategies through parametric modeling, multi-material 3D printing, and mechanical testing, *Adv. Eng. Mater.* 19 (2017).
- [7] F. Barthelat, H. Tang, P.D. Zavattieri, C.-M. Li, H.D. Espinosa, On the mechanics of mother-of-pearl: a key feature in the material hierarchical structure, *J. Mech. Phys. Solids* 55 (2007) 306–337.
- [8] H. Gao, B. Ji, I.L. Jäger, E. Arzt, P. Fratzl, Materials become insensitive to flaws at nanoscale: lessons from nature, *Proc. Natl. Acad. Sci. U.S.A.* 100 (2003) 5597–5600.
- [9] R. Seidel, K. Lyons, M. Blumer, P. Zaslansky, P. Fratzl, J.C. Weaver, M.N. Dean, Ultrastructural and developmental features of the tessellated endoskeleton of elasmobranchs (sharks and rays), *J. Anat.* 229 (2016) 681–702.
- [10] D. Knötel, R. Seidel, S. Prohaska, M.N. Dean, D. Baum, Automated segmentation of complex patterns in biological tissues: Lessons from stingray tessellated cartilage, *PLoS One* 12 (2017) e0188018–24.
- [11] R. Seidel, M. Blumer, E.-J. Pechriggl, K. Lyons, B.K. Hall, P. Fratzl, J.C. Weaver, M. N. Dean, Calcified cartilage or bone? Collagens in the tessellated endoskeletons of cartilaginous fish (sharks and rays), *J. Struct. Biol.* 200 (2017) 54–71.
- [12] M.N. Dean, C.G. Mull, S.N. Gorb, A.P. Summers, Ontogeny of the tessellated skeleton: insight from the skeletal growth of the round stingray *Urobatis halleri*, *J. Anat.* 215 (2009) 227–239.
- [13] J.G. Clement, Re-examination of the fine structure of endoskeletal mineralization in chondrichthyans: implications for growth, ageing and calcium homeostasis, *Aust. J. Mar. Freshw. Res.* 43 (1992) 157–181.
- [14] D. Ashhurst, The cartilaginous skeleton of an elasmobranch fish does not heal, *Matrix Biol.* 23 (2004) 15–22.
- [15] M.N. Dean, J.J. Bizzarro, B. Clark, C.J. Underwood, Z. Johanson, Large batoid fishes frequently consume stingrays despite skeletal damage, *R. Soc. Open Sci.* 4 (2017) 170611–170674.
- [16] S. Wroe, D.R. Huber, M. Lowry, C. McHenry, K. Moreno, P. Clausen, T.L. Ferrara, E. Cunningham, M.N. Dean, A.P. Summers, Three-dimensional computer analysis of white shark jaw mechanics: how hard can a great white bite?, *J. Zool.* 276 (2008) 336–342.
- [17] L.J. Macesic, A.P. Summers, Flexural stiffness and composition of the batoid propterygium as predictors of punting ability, *J. Exp. Biol.* 215 (2012) 2003–2012.
- [18] T.L. Ferrara, P. Boughton, E. Slavich, S. Wroe, A novel method for single sample multi-axial nanoindentation of hydrated heterogeneous tissues based on testing great white shark jaws, *PLoS ONE* 8 (2013) e81196.
- [19] X. Liu, M.N. Dean, H. Youssefpoor, A.P. Summers, J.C. Earthman, Stress relaxation behavior of tessellated cartilage from the jaws of blue sharks, *J. Mech. Behav. Biomed. Mater.* 29 (2014) 68–80.
- [20] J.P. Balaban, A.P. Summers, C.A. Wilga, Mechanical properties of the hyomandibula in four shark species, *J. Exp. Zool. A Ecol. Genet. Physiol.* 323 (2014) 1–9.
- [21] C.A.D. Wilga, S.E. Diniz, P.R. Steele, J. Sudario-Cook, E.R. Dumont, L.A. Ferry, Ontogeny of feeding mechanics in smoothhound sharks: morphology and cartilage stiffness, *Integr. Comp. Biol.* 56 (2016) 442–448.
- [22] A. Atkins, M.N. Dean, M.L. Habegger, P.J. Motta, L. Ofer, F. Repp, A. Shipov, S. Weiner, J.D. Currey, R. Shahar, Remodeling in bone without osteocytes: Billfish challenge bone structure-function paradigms, *Proc. Natl. Acad. Sci.* (2014).
- [23] M.N. Dean, J.J. Socha, B.K. Hall, A.P. Summers, Canalliculi in the tessellated skeleton of cartilaginous fishes, *J. Appl. Ichthyol.* 26 (2010) 263–267.
- [24] S. Omelon, J. Georgiou, F. Variola, M.N. Dean, Colocalization and role of polyphosphates and alkaline phosphatase in apatite biomineralization of elasmobranch tesserae, *Acta Biomater.* 10 (2014) 3899–3910.
- [25] R. Seidel, M. Blumer, P. Zaslansky, D. Knötel, D.R. Huber, J.C. Weaver, P. Fratzl, S. Omelon, L. Bertinetti, M.N. Dean, Ultrastructural, material and crystallographic description of endophytic masses – A possible damage response in shark and ray tessellated calcified cartilage, *J. Struct. Biol.* 198 (2017) 5–18.
- [26] K. Lyons, R. Lavado, D. Schlenk, C.G. Lowe, Bioaccumulation of organochlorine contaminants and ethoxyresorufin-O-deethylase activity in southern California round stingrays (*Urobatis halleri*) exposed to planar aromatic compounds, *Environ. Toxicol. Chem.* 33 (2014) 1380–1390.
- [27] L.F. Hale, C.G. Lowe, Age and growth of the round stingray *Urobatis halleri* at Seal Beach, California, *J. Fish Biol.* 73 (2008) 510–523.
- [28] D. Baum, J.C. Weaver, I. Zlotnikov, D. Knötel, L. Tomholt, M.N. Dean, High-throughput segmentation of tiled biological structures using random walk distance transforms, *Integr. Comp. Biol.* (2019) (in press).
- [29] P. Roschger, E.P. Paschalis, P. Fratzl, K. Klaushofer, Bone mineralization density distribution in health and disease, *Bone* 42 (2008) 456–466.
- [30] N. Hassler, A. Roschger, S. Gamsjaeger, I. Kramer, S. Lueger, A. van Lierop, P. Roschger, K. Klaushofer, E.P. Paschalis, M. Kneissel, S. Papapoulos, Sclerostin deficiency is linked to altered bone composition, *J. Bone Miner. Res.* 29 (2014) 2144–2151.
- [31] P. Roschger, J.H. Plenck, K. Klaushofer, J. Eschberger, A new scanning electron microscopy approach to the quantification of bone mineral distribution: backscattered electron image grey-levels correlated to calcium K alpha-line intensities, *Scanning Microsc.* 9 (1995) 75–86.
- [32] P. Roschger, P. Fratzl, J. Eschberger, K. Klaushofer, Validation of quantitative backscattered electron imaging for the measurement of mineral density distribution in human bone biopsies, *Bone* 23 (1998) 319–326.
- [33] A. Roschger, S. Gamsjaeger, B. Hofstetter, A. Masic, S. Blouin, P. Messmer, A. Berzlanovich, E.P. Paschalis, P. Roschger, K. Klaushofer, P. Fratzl, Relationship between the v2PO4/amide III ratio assessed by Raman spectroscopy and the calcium content measured by quantitative backscattered electron microscopy in healthy human osteonal bone, *J. Biomed. Opt.* 19 (2014), <https://doi.org/10.1117/1.jbo.19.6.065002>.
- [34] N. Fratzl-Zelman, P. Roschger, A. Gourrier, M. Weber, B.M. Misof, N. Loveridge, J. Reeve, K. Klaushofer, P. Fratzl, Combination of nanoindentation and quantitative backscattered electron imaging revealed altered bone material properties associated with femoral neck fragility, *Calcif. Tissue Int.* 85 (2009) 335–343.
- [35] H.S. Gupta, S. Schratler, W. Tesch, P. Roschger, A. Berzlanovich, T. Schoeberl, K. Klaushofer, P. Fratzl, Two different correlations between nanoindentation modulus and mineral content in the bone–cartilage interface, *J. Struct. Biol.* 149 (2005) 138–148.
- [36] D. Labonte, A.-K. Lenz, M.L. Oyen, On the relationship between indentation hardness and modulus, and the damage resistance of biological materials, *Acta Biomater.* 57 (2017) 373–383.
- [37] P.K. Zysset, X. Edward Guo, C. Edward Hoffler, K.E. Moore, S.A. Goldstein, Elastic modulus and hardness of cortical and trabecular bone lamellae measured by nanoindentation in the human femur, *J. Biomech.* 32 (1999) 1005–1012.
- [38] W.C. Oliver, G.M. Pharr, An improved technique for determining hardness and elastic modulus using load and displacement sensing indentation experiments, *J. Mater. Res.* 7 (1992) 1564–1583.
- [39] J.D. Currey, *Bones: Structure and Mechanics*, Princeton University Press, 2002.
- [40] J.D. Hunter, Matplotlib: a 2D graphics environment, *Comput. Sci. Eng.* 9 (2007) 90–95.
- [41] A.K. Jayasankar, R. Seidel, J. Naumann, L. Guiducci, A. Hosny, P. Fratzl, J.C. Weaver, J.W.C. Dunlop, M.N. Dean, Mechanical behavior of idealized, stingray-skeleton-inspired tiled composites as a function of geometry and material properties, *J. Mech. Behav. Biomed. Mater.* 73 (2017) 86–101.
- [42] X. Liu, M.N. Dean, A.P. Summers, J.C. Earthman, Composite model of the shark's skeleton in bending: a novel architecture for biomimetic design of functional compression bias, *Mater. Sci. Eng. C* 30 (2010) 1077–1084.
- [43] P. Fratzl, O. Kolednik, F.D. Fischer, M.N. Dean, The mechanics of tessellations – bioinspired strategies for fracture resistance, *Chem. Soc. Rev.* 45 (2016) 252–267.
- [44] S. Amini, A. Miserez, Wear and abrasion resistance selection maps of biological materials, *Acta Biomater.* 9 (2013) 7895–7907.
- [45] M.M. Barak, J.D. Currey, S. Weiner, R. Shahar, Are tensile and compressive Young's moduli of compact bone different?, *J. Mech. Behav. Biomed. Mater.* 2 (2009) 51–60.

- [46] S.M. Stover, R.R. Pool, R.B. Martin, J.P. Morgan, Histological features of the dorsal cortex of the third metacarpal bone mid-diaphysis during postnatal growth in thoroughbred horses, *J. Anat.* 181 (Pt 3) (1992) 455–469.
- [47] O. Akkus, A. Polyakova-Akkus, F. Adar, M.B. Schaffler, Aging of microstructural compartments in human compact bone, *J. Bone Miner. Res.* 18 (2003) 1012–1019.
- [48] J.D. Currey, M.N. Dean, R. Shahar, Revisiting the links between bone remodelling and osteocytes: insights from across phyla, *Biol. Rev. Camb. Philos. Soc.* 92 (2017) 1702–1719.
- [49] A.C. Fischer-Cripps, *Introduction to Contact Mechanics*, Springer Nature Switzerland AG, 2007.
- [50] R. Shahar, P. Zaslansky, M. Barak, A.A. Friesem, J.D. Currey, S. Weiner, Anisotropic Poisson's ratio and compression modulus of cortical bone determined by speckle interferometry, *J. Biomech.* 40 (2007) 252–264.
- [51] A.A. Espinoza Orías, J.M. Deuerling, M.D. Landrigan, J.E. Renaud, R.K. Roeder, Anatomic variation in the elastic anisotropy of cortical bone tissue in the human femur, *J. Mech. Behav. Biomed. Mater.* 2 (2009) 255–263.
- [52] S. Blouin, S. Puchegger, A. Roschger, A. Berzlanovich, P. Fratzl, K. Klaushofer, P. Roschger, Mapping dynamical mechanical properties of osteonal bone by scanning acoustic microscopy in time-of-flight mode, *Microsc. Microanal.* 20 (2014) 924–936.
- [53] M.N. Dean, L. Ekstrom, E. Monsonogo-Ornan, J. Ballantyne, P.E. Witten, C. Riley, W. Habraken, S. Omelon, Mineral homeostasis and regulation of mineralization processes in the skeletons of sharks, rays and relatives (Elasmobranchii), *Semin. Cell Dev. Biol.* 46 (2015) 51–67.
- [54] S.A. Tont, W.G. Percy, J.S. Arnold, Bone structure of some marine vertebrates, *Mar. Biol.* 39 (1977) 191–196.
- [55] K.B. Clifton, J. Yan, J.J. Mecholsky, R.L. Reep, Material properties of manatee rib bone, *J. Zool.* 274 (2008) 150–159.
- [56] E.R. Dumont, Bone density and the lightweight skeletons of birds, *Proc. R. Soc. B: Biol. Sci.* 277 (2010) 2193–2198.
- [57] S. Lees, E. Page, A study of some properties of mineralized turkey leg tendon, *Connect. Tissue Res.* 28 (1992) 263–287.